ORIGINAL RESEARCH ARTICLE

A Coupled Magnetohydrodynamics (MHD) and Thermal Stress-Strain Model to Explore the Impact of Gas Cooling on Ingot Solidification Shrinkage in Vacuum Arc Remelting (VAR) Process

J. BOHACEK, E. KARIMI-SIBAKI, A. VAKHRUSHEV, K. MRAZ, J. HVOZDA, M. WU, and A. KHARICHA

An advanced 2D axisymmetric magnetohydrodynamics model, including calculations for electromagnetic, thermal, and flow fields, fully coupled with a thermal stress-strain model, allowing the computation of solid mechanical parameters like stress, strain, and deformation within the ingot of the vacuum arc remelting process is presented. This process encounters challenges due to solidification shrinkage, which causes losing contact between the ingot and the mold, reducing the cooling efficiency of the system, resulting in a deeper melt pool and decreasing ingot quality. Herein, the width of the air gap along the ingot, the precise position of contact between the ingot and mold, and the profile of the melt pool, affected by gas cooling, are calculated. The global pattern of transport phenomena, such as (electro-vortex) flow and electromagnetic fields in the bulk of the ingot, is insensitive to helium gas cooling through the shrinkage gap. However, including gas cooling significantly improves heat removal through the mold, which consequently reduces the pool depth of the Alloy 718 ingot, leading to an improvement in the quality of the ingot.

https://doi.org/10.1007/s11663-024-03254-4

I. INTRODUCTION

THE vacuum arc remelting (VAR) process is used to purify various alloys, including stainless steel, nickel-based, and titanium-based alloys. This method refines an impure alloy (the electrode in VAR) within a vacuum environment heated by a DC arc. The tip of the electrode melts, forming droplets that drip through the vacuum into the molten pool. The molten pool solidifies within a water-cooled mold, producing a high-grade, ultra-clean alloy, as illustrated in Figure 1(a). These droplets carry low-density oxide inclusions into the molten pool, which are subsequently transferred to the solidification rim, particularly the surface of the ingot near the mold. Additionally, elements with high vapor pressure, such as Pb, Sn, Bi, Te, As, and Cu, evaporate under vacuum conditions. Some of these elements may condense on the mold wall.[1]

Modeling the VAR process is highly demanding and complex due to the diverse physical phenomena and their interactions. This modeling requires a thorough examination of each phenomenon, including the formation and movement of cathode spots at the electrode tip,[2–4] the dynamics of arc plasma in the vacuum,[3,5,6] the direct transfer of electric current between the electrode and mold (known as "side-arcing"),[7–9] the electrode melting process,[8,10,11] thermal radiation within the vacuum region,[12] and the interaction between turbulent flow and the electromagnetic field (magnetohydrodynamics, MHD) within the molten pool.[1,9,13,14] Additionally, it involves the solidification of the ingot,[1,15] which includes solidification shrinkage that significantly affects energy and electric current transfer between the ingot and mold.

J. BOHACEK, K. MRAZ, and J. HVOZDA are with the Heat Transfer and Fluid Flow Laboratory, Faculty of Mechanical Engineering, Brno University of Technology, Technicka 2896/2, 616 69 Brno, Czech Republic. E. KARIMI-SIBAKI and A. KHARICHA are with the Christian-Doppler Laboratory for Metallurgical Applications of Magnetohydrodynamics Montanuniversitaet Leoben, Franz-Josef-Str. 18, 8700 Leoben, Austria, and also with the Chair of Simulation and Modeling of Metallurgical Processes, Montanuniversitaet Leoben, Franz-Josef-Str. 18, A-8700 Leoben, Austria. Contact e-mail: abdellah.kharicha@unileoben.ac.at A. VAKHRUSHEV is with the Christian-Doppler Laboratory for Metallurgical Applications of Magnetohydrodynamics, Montanuniversitaet Leoben. M. WU is with the Chair of Simulation and Modeling of Metallurgical Processes, Montanuniversitaet Leoben.
Manuscript submitted July 4, 2024; accepted August 12, 2024.

Published online: 04 September 2024

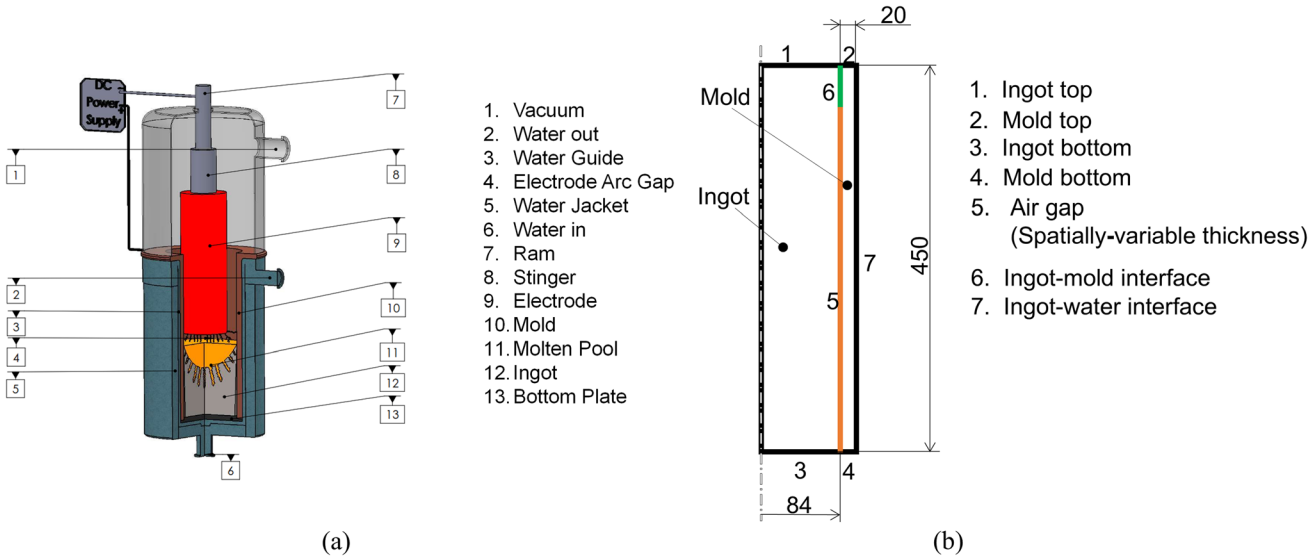

Fig. 1—(*a*) Schematic representation of the VAR process, (*b*) 2D axisymmetric computational domain of the VAR process, including ingot and mold regions, boundaries and dimensions in millimeters..

Limited research has been conducted on the solidification shrinkage in VAR ingots,[16] making this a particularly complex topic due to its involvement with both fluid and solid mechanics. To address this issue, it is necessary to consider the interaction between flow, thermal, and magnetic fields in the molten pool to accurately determine the pool profile and thermal field throughout the ingot. Additionally, a comprehensive thermal stress-strain model is essential for calculating solid mechanical parameters such as stress, strain, and deformation within the ingot.[17]

In the present study, we propose a model that integrates the previously mentioned phenomena, encompassing both solid and fluid mechanics. The variation in the cooling efficiency of the mold as a consequence of the injection of Helium gas in the shrinkage gap is also modeled. The aim is to develop a foundational understanding of solidification shrinkage in the as-cast ingot and its implications for the overall transport phenomena in the VAR process.

II. MODEL

A. *MHD and Thermal Fields*

We consider a 2D axisymmetric computational domain that includes both the ingot and the mold. Using the finite volume method (FVM), we model turbulent flow, temperature, and electromagnetic fields. To simplify and reduce complexity, we apply the following assumptions[1]:

(i) We assume the ingot's top, which is directly exposed to the plasma arc, is stationary and flat. The impact of the arc is implicitly incorporated by considering a Gaussian distribution of electric current density on the ingot's top.

(ii) The electrode, mold, ingot, and arc engage in complex radiative heat exchange within the vacuum. Given the minimal diameter difference between the electrode and ingot in VAR, we simplify the calculation using the Stefan-Boltzmann law with an emissivity coefficient of 0.9 to determine the radiation heat transfer rate from the electrode tip to the ingot top. Experimental measurements indicate that the electrode tip temperature is approximately 150 K above the alloy's liquidus.[13]

(iii) The tracking of droplet formation at the electrode tip and their dripping into the vacuum zone is not included in the model. Since droplets contribute mass, energy, and momentum to the melt pool, source terms are added to the governing equations of continuity, momentum, and energy to implicitly account for their impact on transport phenomena in the melt pool. Detailed derivations and formulas for these source terms are provided in Reference 18.

(iv) At the top edge of the ingot near the mold, where the alloy remains in a 'soft' or liquid state, an initial contact length of 30 mm is generally assumed in the literature.[1] Below this contact zone, the ingot shrinks away from the mold, forming an air gap, as shown in Figure 1(b). The coupled calculation with the thermal stress-strain model allows us to directly compute the contact length, which will be further described in the following.

To avoid making this paper long-winded, the governing equations and corresponding boundary conditions related to flow, magnetic field, and thermal/solidification are not presented. They are extensively described in Reference 1. In a nutshell, the vector potential formulation, including magnetic vector potential ($\vec{A}$) and electric scalar potential (φ), is applied to compute the electromagnetic field across the entire

domain.[1] After computing the magnetic field ($\vec{B}$), the Lorentz force ($\vec{F}_L$) is calculated and added as a source term to the momentum equations.[1,9] The turbulent flow field in the melt pool is computed using the scale-adaptive simulation (SAS) approach to model turbulence. The drag resistance of the dendritic mushy zone to the flow is accounted for using the Kozeny-Carman permeability model.[1,13] The thermal field is modeled by solving an enthalpy (h) conservation equation, including solidification Latent heat. Interested readers are highly encouraged to consult Reference 1 for further details.

Herein, special care must be taken to model the thermal boundary condition at the interface between the mold and ingot, where adequate thermal boundaries are ensured by providing continuity of temperature and heat flux.[19] According to Reference 20, the edge or outer surface of a VAR ingot is where the metal solidifies first and is, therefore, alloy-lean, sometimes referred to as the shelf. In addition to being alloy-lean, the shelf is composed of nitrides, oxides, and vapor deposits that form a thermal barrier to heat transfer.

Two heat transfer zones are distinguished along the length of the ingot, including the contact and the gap, as shown in Figure 1(b). Herein, the thermoelastic model predicts the gap width along the vertical direction as well as a theoretical contact between ingot and mold. Thereby, the heat transfer through the shelf (contact zone) is modeled by a finite heat transfer coefficient, $h_{contact}$, of approximately 500 Wm^{-2} K^{-1}.[1,11,13] Accordingly, the heat flux at the conjugate wall, $q_{contact}$, is dependent on temperature at mold side, $T_{w,mold}$, and ingot side, $T_{w,ingot}$, as follows:

$$q_{contact} = h_{contact} \cdot \left(T_{w,mold} - T_{w,ingot}\right) \quad [1]$$

In the second zone, as the ingot shrinks, contact with the mold is lost and the gap forms. The resulting heat flux, q_{gap}, is the sum of the conduction and radiation, which can be written as follows:

$$q_{gap} = \frac{1}{\frac{1}{h_{gap}} + \frac{1}{h_{contact}}} \cdot \left(T_{w,mold} - T_{w,ingot}\right) + \varepsilon\sigma\left(T^4_{w,mold} - T^4_{w,shelf}\right) \quad [2]$$

In which ε and σ denote the emissivity and the Stefan-Boltzmann constant. Non-linear Eq. [2] contains $T_{w,shelf}$, which can be understood as $T_{w,ingot} - q_{gap}/h_{contact}$. In the absence of gas cooling, the term involving heat transfer coefficient, h_{gap}, in the gap is omitted. Contrastingly, when a pressurized noble gas is used in the gap, the conductive heat transfer coefficient, h_{gap}, becomes vital. Denoting the gap width as δ, in the conductive limit $h_{cl,gap}$ is given by:

$$h_{cl,gap} = \frac{\lambda_{gap}}{\delta} \quad [3]$$

λ_{gap} denotes the thermal conductivity of the cooling gas in the gap. When the gap reduces to the mean-free path of the gas molecules, h_{gap} is approximated by the well-known problem of the Boltzmann equation and heat transfer between parallel plates in the context of rarefied gas dynamics.[21]

Helium pressure, P, in the gap is known (here 40 mmHg or 5333 Pa). The dynamic viscosity, μ_{He}, was determined using an empirical function as

$$\mu_{He} = 1.865 \cdot 10^{-5} \cdot \left(\frac{T_{He}}{273.16}\right)^{0.7} \quad [4]$$

in which T_{He} is the gas temperature in Kelvin.[22] The mean-free path of the gas molecules, denoted as l, can be expressed by the following equation:

$$l = \frac{\mu_{He}}{P} \cdot \left(\frac{\pi R T_{He}}{2M}\right)^{0.5} \quad [5]$$

The symbol M refers to the molar mass of Helium, and R is the universal gas constant. The mean-free path, l, and the gap width, δ, are used to determine the Knudsen number as $\mathrm{Kn} = l/\delta$. When the gap width, δ, is close to zero, the heat transfer coefficient, h_{gap}, reaches the so-called free molecular limit, which is found below the conductive limit, and is defined as follows:

$$h_{0,gap} = 0.25 \cdot \frac{\gamma + 1}{\gamma - 1} P \left(\frac{2R}{\pi M T_{He}}\right)^{0.5} \quad [6]$$

γ is the adiabatic constant, $\gamma = \frac{c_p}{c_v}$, and c_p and c_v are respectively specific heat at constant pressure and constant volume. In the transition from the statistical to continuum gas dynamics, i.e., as the Knudsen number, Kn, decreases, the heat transfer coefficient, h_{gap}, between the free molecular limit, Eq. [3] and the conductive limit, Eq. [6], is expressed as,

$$h_{gap} = 0.5 \cdot h_{0,gap} \left(\frac{1}{1 + 1/(\chi \cdot \mathrm{Kn})} + \frac{1}{\left(1 + (1/\chi \cdot \mathrm{Kn})^{0.5}\right)^2}\right) \quad [7]$$

In which the constant, χ, is calculated as follows:

$$\chi = \frac{2(\pi)^{0.5}}{3} \frac{9\gamma - 5}{\gamma + 1} \quad [8]$$

The above procedure for calculating h_{gap} near the free molecular limit is described in detail in Refs. [23, 24].

B. *Thermal Stress-Strain Model*

The deformation of the ingot due to changes in the temperature field is described by the equations of linear elasticity, derived for axial symmetry using polar coordinates r, φ, z. A similar approach has been adopted in Refs. [16, 25]. The equilibrium of forces is described by two partial differential equations of equilibrium as follows:

$$\frac{\partial \sigma_r}{\partial r} + \frac{\partial \tau_{rz}}{\partial z} + \frac{1}{r}\left(\sigma_r - \sigma_\varphi\right) = 0 \quad [9]$$

$$\frac{\partial \tau_{rz}}{\partial r} + \frac{1}{r}\tau_{rz} + \frac{\partial \sigma_z}{\partial z} = 0 \quad [10]$$

where σ_r, σ_φ, σ_z and τ_{rz} stand for radial, tangential, axial and shear stress, respectively. The relationship between stresses and strains is established through four equations of constitutive relations:

$$\sigma_r = \frac{E}{1-2v}\left[\frac{1-v}{1+v}\varepsilon_r + \frac{v}{1+v}\left(\varepsilon_\varphi + \varepsilon_z\right) - \alpha_T T\right] \quad [11]$$

$$\sigma_\varphi = \frac{E}{1-2v}\left[\frac{1-v}{1+v}\varepsilon_\varphi + \frac{v}{1+v}\left(\varepsilon_r + \varepsilon_z\right) - \alpha_T T\right] \quad [12]$$

$$\sigma_z = \frac{E}{1-2v}\left[\frac{1-v}{1+v}\varepsilon_z + \frac{v}{1+v}\left(\varepsilon_r + \varepsilon_\varphi\right) - \alpha_T T\right] \quad [13]$$

$$\tau_{rz} = \frac{E}{(1+v)}\varepsilon_{rz} \quad [14]$$

The last term in the first three equations accounts for the thermal strain caused by thermal expansion or shrinkage. T stands for the temperature relative to the solidus temperature of the alloy. Four geometric equations (three differential, one algebraic) relate strain with displacement as follows:

$$\begin{cases} \varepsilon_r = \frac{\partial w_r}{\partial r}, \\ \varepsilon_\varphi = \frac{w_r}{r}, \\ \varepsilon_z = \frac{\partial w_z}{\partial z}, \\ \varepsilon_{rz} = \frac{1}{2}\left(\frac{\partial w_z}{\partial r} + \frac{\partial w_r}{\partial z}\right). \end{cases} \quad [15]$$

Boundary conditions related to the thermal stress-strain model are shown schematically in Figure 2. Frictionless support at the bottom (ingot bottom), free surface at the top (ingot top), and free surface at the right side (ingot-mold interface and air gap) are equivalent comparing Figures 1(b) and 2.

No external force or pressure field exists. Thus, variation in the thermal field provides the only acting load. The governing equations, Eqs. [9] and [10], were solved using the finite difference method (FDM). For that purpose, the thermoelastic model was implemented in an in-house FDM code. Within the FDM code, the computational domain was discretized into a uniform grid of computational nodes, as shown in Figure 2. The first and second derivatives were substituted by central differences as follows:

$$\begin{cases} \frac{\partial w}{\partial r} = \frac{w_{i+1} - w_{i-1}}{2\Delta l} \\ \frac{\partial^2 w}{\partial r^2} = \frac{w_{i+1} - 2w_i + w_{i-1}}{\Delta l^2} \end{cases} \quad [16]$$

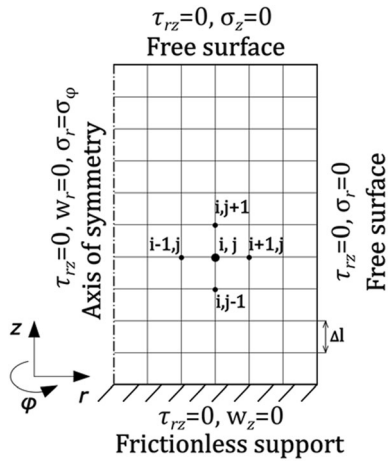

Fig. 2—Schematic of the computational domain for the in-house FDM code, including node indexing and boundary conditions.

The unknown stresses in Eqs. [9] and [10] were substituted by strains from Eqs. [11] through [14]. Also, displacements in radial and axial directions are included through Eq. [15]. Therefore, two algebraic equations with two unknown w_r,w_z were formulated for each computational node. The final set of equations can be expressed in the matrix form,

$$\boldsymbol{A}\boldsymbol{w} = \boldsymbol{b} \quad [17]$$

where $\boldsymbol{A}$ is the coefficients matrix with dimensions $2n \times 2n$, with n being the number of computational nodes. The vector of unknowns, $\boldsymbol{w}$, consists of displacements denoted w_r and w_z. The vector of loads is denoted by $\boldsymbol{b}$. The schematic picture of the computational domain considering the in-house FDM code is shown in Figure 3. The distance between computational nodes Δl in both radial and axial direction is 2 mm, which resulted in the computational mesh with 43 × 226 nodes, correlating with the physical size of 84 × 450 mm of the ingot. Our simulation trials, considering a convergence study of our in-house FDM code, revealed that further reducing Δl has negligible effect on displacement results.

The system of linear equations, Eq. [17], was solved for the displacements $\boldsymbol{w}$ using a direct solver based on the LU decomposition. All required quantities, such as strains and stresses, can be calculated using $\boldsymbol{w}$ through Eqs. [11] through [15]. Afterwards, the computed parameters are used for the coupling with the MHD model in ANSYS FLUENT, as shown in Figure 3. For that purpose, the Schwartz alternating method was used. Thus, the entire computation was carried out by a shell script, repeatedly launching FLUENT and the in-house FDM code. Temperature values in the nodes of the ingot, calculated by the fluid flow model, were used as input for the thermoelastic model. Concurrently, the vector of gap width, $\boldsymbol{\delta}$, calculated by the thermoelastic model, was used as an input for the MHD model. The fully coupled calculations continue to achieve steady-state results.

A summary of averaged values considering the temperature-dependent parameters used in the MHD simulation is listed in Table I.

In addition, material properties present in the governing equations of the thermoelastic model are Young's modulus E, Poisson's ratio v and coefficient of thermal expansion α_T. They are also temperature-dependent and approximated by polynomial functions, as shown in Figure 4.

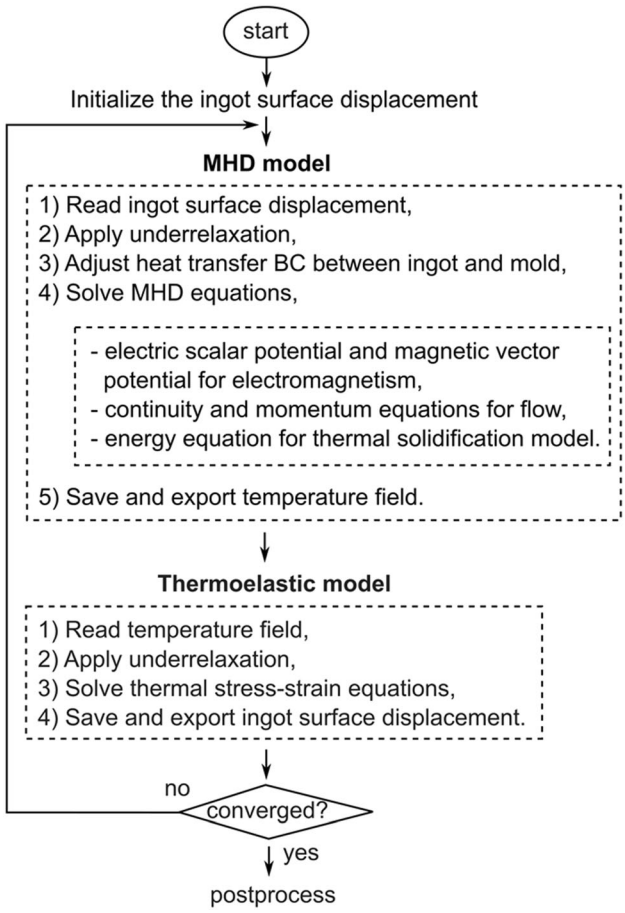

Fig. 3—The flowchart of coupling between the thermoelastic model and the MHD model.

III. RESULTS AND DISCUSSION

A. *In-house FDM Code Verification*

As shown in Figure 5(a), the position of the first contact between the ingot and the mold, further referred to as $\min(z)$, was used as a convergence criterion during the Schwartz alternating method in our coupled MHD-stress-strain model. Considering the ingot height of 450 mm, the contact length can be calculated as $450 - \min(z)$. The calculated contact lengths (a few centimeters) were in the range of values reported in the literature.[1,26]

To the best of our knowledge, there exists no direct experimental measurements or analytical solution for the shrinkage gap width. The ability of our in-house FDM code was verified against the commercial software ANSYS APDL 2024 R1, considering the same number of elements in the ingot. The APDL software requires only the thermal field to calculate stress-strain results. The radial deformation of the ingot surface simulated by both solvers is shown in Figure 5(b). The calculated gap width is a result of ingot shrinkage along the entire length of the ingot. The maximum shrinkage is predicted at the bottom of the ingot near the baseplate. The gap width gradually decreases from the bottom to the top of the ingot. When the ingot comes into full contact with the mold, the gap width becomes zero.

As shown in Figure 5(b), the results only slightly differ at the top surface. Quadratic eight-node elements used in APDL result in more accurate outcomes compared to the second-order central differences considered in the in-house FDM code. Nevertheless, the calculated contact length at the ingot-mold interface (i.e., zero shrinkage gap) is nearly identical. In Figure 5(b), the contact length difference is smaller than 3 pct, which indicates that the in-house FDM code is capable of replicating results using the commercial software ANSYS APDL 2024 R1.

B. *Transport Phenomena*

To explore the influence of gas cooling, in the present work, two simulations were carried out: (i) without gas cooling and (ii) with Helium gas injected into the shrinkage gap with pressure of 40 mmHg (5333 Pa).

Table I. A Summary of Parameters Used in the Simulation for Inconel 718

Material Properties and Composition		Operation Parameters	
Density (kg m^{-3})	7491	ingot diam. (mm)	168
Viscosity (Pa s)	0.005	elec. diam. (mm)	108
Specific heat (J kg^{-1})	427–700	ingot length (mm)	450
Thermal Cond. (W m^{-1} k^{-1})	11–32	melt rate (kg hr^{-1})	113
Liq. Therm. Exp. Coeff. (K^{-1})	0.000012	current (kA)	3
Liquidus Temperature (K)	1609	gap length (mm)	15
Solidus Temperature (K)	1533	gas pressure (mmHg)	40
Electrical Cond. (S m^{-1})	1×10^6		
Ni 52.5 pct, Fe 18.5 pct, Cr 19 pct, Cb + Ta 5.13 pct, Mo 3.05 pct, Ti 0.9 pct, Al 0.5 pct			

Helium is a high-heat-capacity gas used to improve heat removal from solidifying and shrinking ingots. The application of Helium gas enables us to operate the process using a high melt rate, while achieving an ingot with shallow pool depth. This helps to maintain directional solidification of dendrites growing parallel to the ingot axis and, ultimately, the high quality of the product. All other parameters are identical and listed in Table I.

The calculated transport phenomena in the melt pool and ingot without gas cooling are shown in Figures 6(a) and (b). To demonstrate the pool profile, isolines of liquid fractions 0.98 and 0.07 are used. As shown in Figure 6(a), the current density is intense in the vicinity of the top of the ingot and the position of the contact.[1] Lorentz force is generally directed towards the center of the ingot, except near the top, where the force is directed downwards. The Lorentz force is stronger than the buoyancy force, which acts in the opposite direction. Thus, the flow in the melt pool is dominated by the Lorentz force. This leads to the formation of an electro-vortex flow, as shown in Figure 6(b). The thermal field remains relatively uniform because of intensive stirring in the melt pool. However, the hot melt can travel a longer distance due to the strong axial flow near the center of the ingot that, in turn, increases the depth of the melt pool.

Figures 6(c) and (d) illustrate results, including the gas cooling. The global transport phenomena resemble the results without gas cooling. As such, the peak current density and Lorentz force are near the top of the ingot. The flow in the melt pool also is electro-vortex. Contrastingly, a shallower pool depth is predicted using Helium cooling compared to the process operated without gas cooling. This implies that heat removal efficiency through the mold is significantly improved using gas cooling.

Note that the contact length, which typically takes values around 20–30 mm,[1,26] is a crucial and self-adjusting parameter. In the present study, the simulated contact lengths were 13 and 17 mm for the case without gas cooling and the case with Helium, respectively. Through the contact, the current density $\boldsymbol{j}$ enters the ingot and heat conduction is the only mechanism of heat

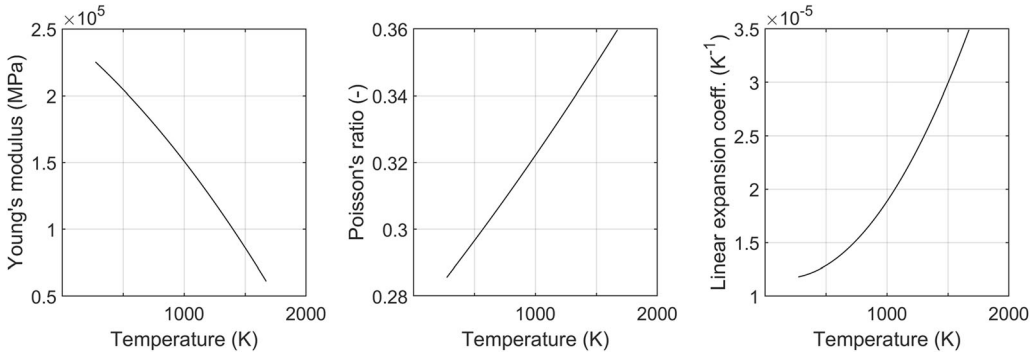

Fig. 4—Temperature-dependent material properties related to the thermoelastic model.

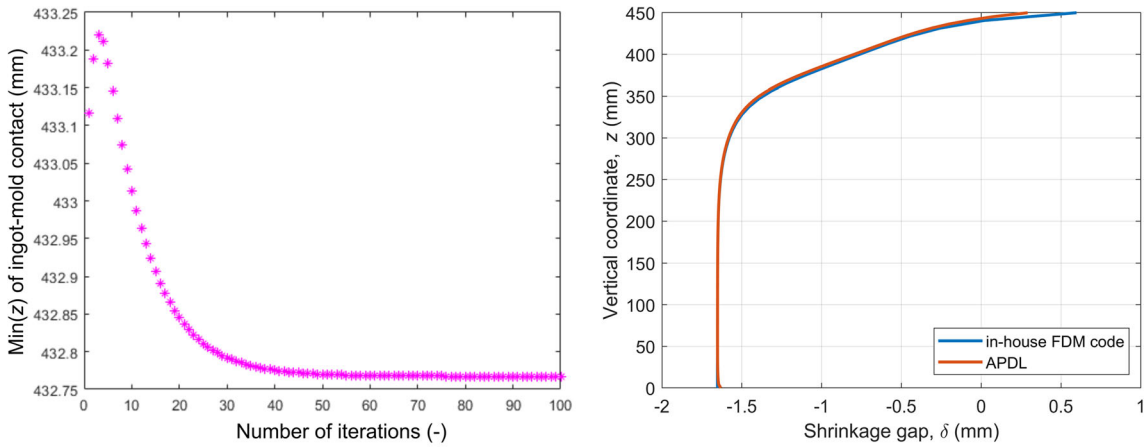

Fig. 5—(*a*) Convergence of the Schwartz alternating method coupling the thermoelastic model with the MHD thermal fluid flow model. (*b*) Comparison of results using the in-house FDM code and the commercial ANSYS APDL 2024 R1.

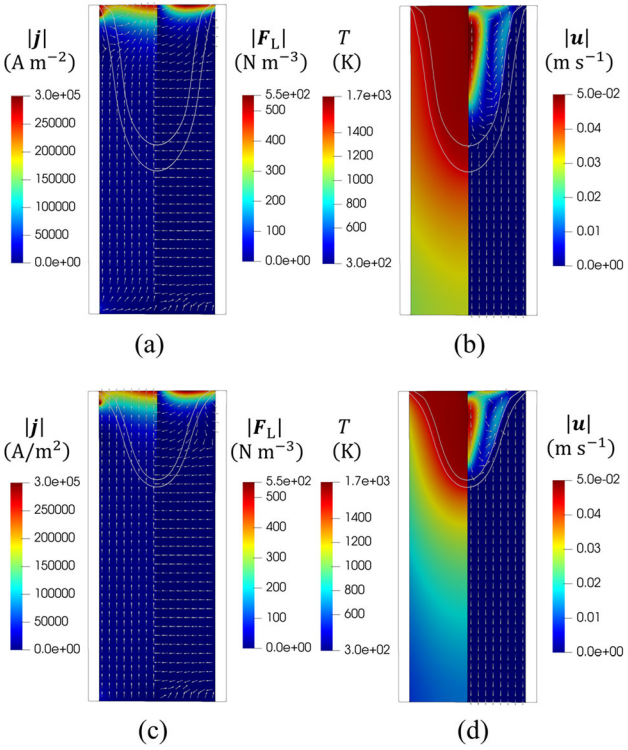

Fig. 6—Current density $|\boldsymbol{j}|$, Lorentz force $|\boldsymbol{F}_L|$, Temperature T, velocity $|\boldsymbol{u}|$ in the ingot (*a–b*) without gas cooling, (*c–d*) Helium gas cooling. Isolines of liquid fraction ($f_l = 0.07$ and 0.98) are also inserted.

transfer. When the contact is lost, i.e. shrinkage appears, heat conduction is blocked, and only radiative heat transfer exists. The width of the shrinkage gap δ, which varies along the length of the ingot, plays a pivotal role once Helium gas is injected into the gap, considering Eq. [3]. Despite surpassing the free molecular limit because of small δ, conductive heat transfer once again becomes a dominant heat transfer mechanism in the shrinkage gap and makes ca. 80 pct of the overall heat transfer as described in Eq. [2].

C. *Solidification Shrinkage*

While the drop of temperature with respect to the reference temperature (the solidus temperature), along with the coefficient of thermal expansion, is the only factor that contributes to the shrinkage or a relative change of the volume, the total deformation and the resulting shape of the ingot are governed by the equilibrium of forces (Eqs. [9] and [10]). Therefore, stress modeling is essential to accurately predict the spatially variable gap width and the contact length.

Results related to the thermal stress-strain model, such as displacements, stresses and strains in the ingot, are shown in Figure 7. They are relevant in the solidified part of the ingot, below 0.07 liquid fraction. It should be noted that only the ingot was subjected to the deformation caused by the thermal load. Mold deformation was assumed to be negligible due to the relatively homogeneous and uniform temperatures of cooling water. Figures 7(a) through (d) illustrates results without gas cooling, whereas Figures 7(e) through (h) shows results with Helium gas cooling. Negative values of w_r and w_z represent shrinkage, i.e. the formation of the gap. Negative and positive values of normal stresses σ represent compression and tension, respectively. The peak value of axial stress σ_z as shown in Figures 7(b) and (f) near the axis of the ingot, is attributed to the bending of the upper part of the solidified ingot, where the presence of an abundant amount of liquid melt facilitates shrinkage. Despite the presence of intense stress near the axis, the ingot temperature remains high (above 1000°C), where the viscous effects are still significant, which results in the relaxation of the elastic stress in the material. This can be identified from the distribution of radial and axial elastic strains, ε_r and ε_z, as shown in Figures 7(d) and (h).

A comparison is made between results without gas cooling shown in Figures 7(a) through (d) and those with Helium gas cooling shown in Figures 7(e) through (h). Deformations, stresses, and strains become more potent when Helium gas cooling is applied. This is due to the intensification of thermal load as a consequence of improving the efficiency of heat dissipation to the mold. Higher temperature differences between maximum and minimum temperature (1000°C for the case with Helium cooling *vs* 600°C for the case without gas cooling) are observed as well as higher temperature gradients (10000°C/m *vs* 5000°C/m). The differences in thermal load between the two cases define the differences in mechanical quantities proportionally.

The experimental results of the pool profile reported by Hosamani[27,28] are used to validate our modeling results, as shown in Figure 8. In the experiments, Nickel particles were used to mark the pool profile.[27,28] Figure 8(a) demonstrates the experimental pool profile without gas cooling, whereas Figure 8(b) illustrates the results when Helium gas cooling was applied. The modeling result reasonably agrees with the experimental results, as shown in Figure 8(c). The calculated pool profile is illustrated using isolines of liquid fractions of 0.07 and 0.98.

This study aims to aid the industry in analyzing an industry ingot with a marked pool shape compared to the simulation results. The importance of applying gas cooling on the outcome of the VAR process, including transport phenomena, stress, strain, and shrinkage of the as-solidified ingot, is highlighted.

IV. SUMMARY

The vacuum arc remelting (VAR) process is used to produce nickel-based alloys, including Alloy 718. A 2D axisymmetric magnetohydrodynamics (MHD) model, coupled with a thermal stress-strain model, is proposed to capture transport phenomena within the ingot, including solidification shrinkage. This model enables the computation of flow, thermal, and electromagnetic fields by considering both the ingot and mold in the VAR process. The model also predicts crucial parameters such as stress, strain, deformation, the position of

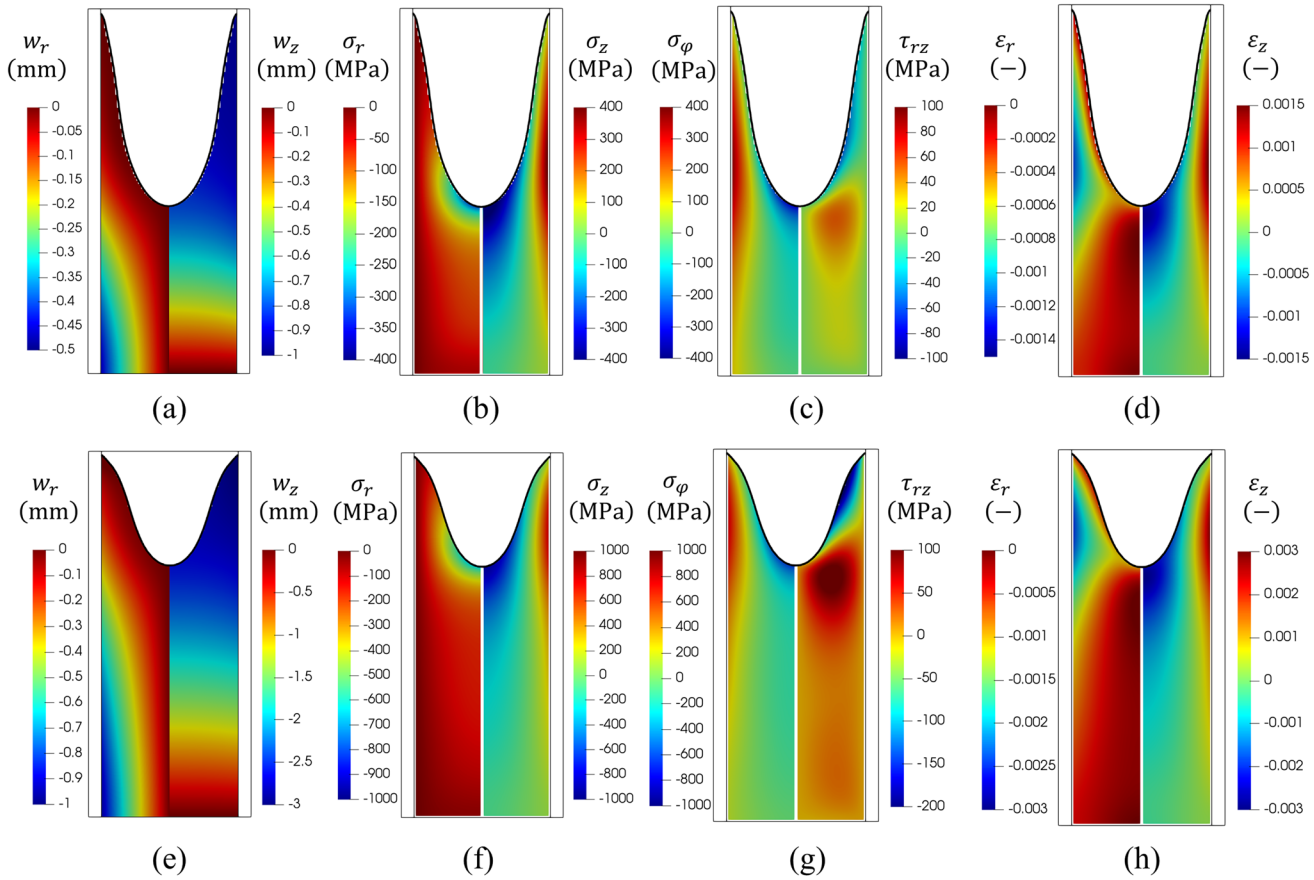

Fig. 7—Deformations, stresses and strains in the ingot without gas cooling (*a–d*) and with Helium gas cooling (*e–h*).

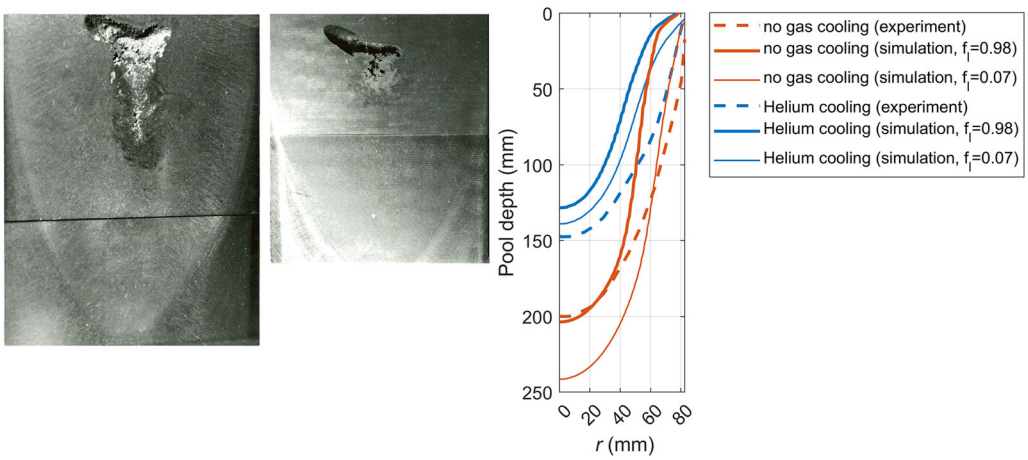

Fig. 8—(*a*) Experimental pool profile without gas cooling and (*b*) with Helium gas cooling; (*c*) Simulated pool shapes using liquid fractions of 0.07 and 0.98 compared to the experiment extracted from Reference 27, 28 available under Creative Commons By Attribution 4.0 in: https://creativecommons.org/licenses/by/4.0/.

contact at the ingot-mold interface, and the gap width due to shrinkage of the ingot. They are critical parameters that influence heat removal from the ingot, the depth of the melt pool, and, ultimately, the quality of the final product. The influence of applying Helium gas cooling, injected into the gap between ingot and mold on the aforementioned parameters, is also studied. Gas cooling has minimal effect on the global pattern of transport phenomena such as flow, thermal, and electromagnetic fields. However, gas cooling significantly

improves heat removal through the mold, which in turn leads to a notable decrease in the depth of the melt pool. Modeling results are validated against an experiment.

ACKNOWLEDGMENTS

The authors acknowledge financial support from the Austrian Federal Ministry of Economy, Family and Youth and the National Foundation for Research, Technology and Development within the framework of the Christian-Doppler Laboratory for Metallurgical Applications of Magnetohydrodynamics. The paper presented has also been partially supported by the internal grant of the Brno University of Technology focused on specific research and development No. FSI-S-23-8254.

CONFLICT OF INTEREST

On behalf of all authors, the corresponding author states that there is no conflict of interest.

FUNDING

Open access funding provided by Montanuniversität Leoben.

OPEN ACCESS

NOMENCLATURES

$\underline{\boldsymbol{A}}$	Coefficient matrix, MPam^{-2}
$\overrightarrow{A}$	Magnetic vector potential,V s m^{-1}
$\underline{\boldsymbol{b}}$	Vector of loads, MPam^{-1}
$\overrightarrow{B}$	Magnetic field, T
c_p	Specific heat at constant pressure, J kg^{-1}K^{-1}
c_v	Specific heat at constant volume, J kg^{-1}K^{-1}
$\underline{E}$	Young's modulus
$\overrightarrow{E}$	Electric field,V m^{-1}
$\overrightarrow{F}_L$	Volumetric Lorentz force, N m^{-3}
$h_{contact}$	Heat transfer coefficient through the shelf (contact zone), W m^{-2}K^{-1}
$h_{cl,gap}$	Heat transfer coefficient through the gap in the conductive limit, W m^{-2}K^{-1}
$h_{0,gap}$	Heat transfer coefficient in the free molecular limit, W m^{-2}K^{-1}
h_{gap}	Heat transfer coefficient between the conductive limit and the free molecular limit, W m^{-2}K^{-1}
h	Enthalpy, J kg^{-1}
$\underline{\mathrm{I}}$	Imposed electrical current, A
$\overrightarrow{\mathrm{j}}$	Electric current density, A m^{-2}
l	Mean-free path of gas molecules, m
Kn	Knudsen number, -
M	Molar weight, kgmol^{-1}
n	Number of computational nodes in the in-house FDM code, -
P	Gas pressure, Pa
$q_{contact}$	Heat flux through the shelf (contact zone), W m^{-2}
q_{gap}	Heat flux through the gap (shrinkage zone), W m^{-2}
R	Universal gas constant, 8.314 J K^{-1}mol^{-1}
r	Radial coordinate, m
T	Temperature, K
T_{He}	Temperature of Helium, K
$T_{w,ingot}$	Wall temperature of the ingot, K
$T_{w,mold}$	Wall temperature of the mold, K
$T_{w,shelf}$	Shelf temperature on the mold side, K
$\overrightarrow{\mathrm{u}}$	Velocity vector, m s^{-1}
$\boldsymbol{w}$	Vector of unknowns (radial and axial displacements), m
z	Axial coordinate, m
α_T	Thermal expansion coefficient, K^{-1}
γ	Adiabatic constant, -
δ	Gap width, m
Δl	Node spacing of a regular grid, m
ε	Emissivity, -
ε_r	Radial strain, -
ε_φ	Tangential strain, -
ε_z	Axial strain, -
λ	Thermal conductivity, W K^{-1}m^{-1}
ρ	Density, kg m^{-3}
σ	Stefan-Boltzmann constant, 5.67 W m^{-2}K^{-4}
λ_{gap}	Thermal conductivity of the cooling gas in the gap, W m^{-1}K^{-1}
μ_{He}	Dynamic viscosity of Helium, kg m^{-1}s^{-1}
μ	Viscosity, kg s^{-1}m^{-1}
φ	Electric potential, V
ν	Poisson's ratio, -
σ	Electrical conductivity, S m^{-1}
σ_r	Radial stress, MPa
σ_φ	Tangential stress, MPa
σ_z	Axial stress, MPa
τ_{rz}	Shear stress, MPa

REFERENCES

1. E. Karimi-Sibaki, A. Kharicha, M. Wu, A. Ludwig, and J. Bohacek: *Metall. Mater. Trans. B*, 2020, vol. 51, pp. 222–35.

2. A. Anders: *Cathodic Arcs: From Fractal Spots to Energetic Condensation*, Springer, New York, 2008.
3. B. Tezenas du Montcel, P. Chapelle, C. Creusot, and A. Jardy: *IEEE Trans. Plasma Sci.*, 2018, vol. 46, pp. 3722–30.
4. A.M. Chaly, A.A. Logatchev, and S.M. Shkol'nik: *IEEE Trans. Plasma Sci.*, 1997, vol. 25, pp. 564–70.
5. P. Chapelle, H. El Mir, J.P. Bellot, A. Jardy, D. Ablitzer, and D. Lasalmonie: *J. Mater. Sci.*, 2004, vol. 39, pp. 7145–52.
6. E. Karimi-Sibaki, M. Peyha, A. Vakhrushev, M. Wu, A. Ludwig, J. Bohacek, B. Preiss, and A. Kharicha: *Sci. Rep.*, 2022, vol. 12, p. 20405.
7. M. Cibula, P. King, and J. Motley: *Metall. Mater. Trans. B*, 2020, vol. 51, pp. 2483–91.
8. R.L. Williamson, F.J. Zanner, and S.M. Grose: *Metall. Mater. Trans. B*, 1997, vol. 28, pp. 841–53.
9. E. Karimi-Sibaki, A. Kharicha, M. Abdi, A. Vakhrushev, M. Wu, A. Ludwig, and J. Bohacek: *Metall. Mater. Trans. B*, 2021, vol. 52, pp. 3354–62.
10. F.J. Zanner, L.A. Bertram, R. Harrison, and H.D. Flanders: *MTB*, 1986, vol. 17, pp. 357–65.
11. H.E. Mir, A. Jardy, J.P. Bellot, P. Chapelle, D. Lasalmonie, and J. Senevat: *J. Mater. Process. Technol.*, 2010, vol. 210, pp. 564–72.
12. P.O. Delzant, B. Baqué, P. Chapelle, and A. Jardy: *Metall. Mater. Trans. B*, 2018, vol. 49, pp. 958–68.
13. E. Karimi-Sibaki, A. Kharicha, A. Vakhrushev, M. Abdi, M. Wu, A. Ludwig, J. Bohacek, and B. Preiss: *J. Market. Res.*, 2022, vol. 19, pp. 183–93.
14. A. Patel and D. Fiore: *IOP Conf. Ser. Mater. Sci. Eng.*, 2016, vol. 143, p. 012017.
15. J. Cui, B. Li, Z. Liu, Y. Xiong, F. Qi, Z. Zhao, and S. Zhu: *Metall. Mater. Trans. B*, 2023, vol. 54, pp. 661–72.
16. M. Eickhoff, N. Giesselmann, A. Rückert, H. Pfeifer, J. Tewes, J. Klöwer, in 2nd International Conference ICRF 2014, Milan, 2014.
17. A. Vakhrushev, M. Wu, A. Ludwig, Y. Tang, G. Hackl, and G. Nitzl: *IOP Conf. Ser. Mater. Sci. Eng.*, 2012, vol. 33, p. 012014.
18. E. Karimi-Sibaki, A. Kharicha, M. Wu, A. Ludwig, J. Bohacek, H. Holzgruber, B. Ofner, A. Scheriau, and M. Kubin: *Appl. Therm. Eng.*, 2018, vol. 130, pp. 1062–69.
19. J. Bohacek, A. Kharicha, A. Ludwig, M. Wu, and E. Karimi-Sibaki: *Metall. Mater. Trans. B*, 2018, vol. 49, pp. 1421–33.
20. S. Viswanathan, D. Apelian, R.J. Donahue, B. DasGupta, M. Gywn, J.L. Jorstad, R.W. Monroe, M. Sahoo, T.E. Prucha, and D. Twarog, eds.: *Casting*, ASM International, 2008, pp. 132–38.
21. S.A. Schaaf: *Modern Developments in Gas Dynamics: Based upon a course on Modern Developments in Fluid Mechanics and Heat Transfer, Given at the University of California at Los Angeles*, Springer, Boston, 1969, pp. 235–54.
22. H. Petersen: *Properties of Helium: Density, Specific Heats, Viscosity, and Thermal Conductivity at Pressures From 1 to 100 Bar and From Room Temperature to About 1800 K*, Forskningscenter Risoe, Denmark, 1970.
23. A.V. Gusarov and E.P. Kovalev: *Phys. Rev. B*, 2009, vol. 80, 024202.
24. A.V. Gusarov: *AIP Conf. Proc.*, 2005, vol. 762, pp. 294–99.
25. M.K. Alam, S.L. Semiatin, and Z. Ali: *J. Manuf. Sci. Eng.*, 1998, vol. 120, pp. 755–63.
26. K. Pericleous, G. Djambazov, M. Ward, L. Yuan, and P.D. Lee: *Metall. Mater. Trans. A*, 2013, vol. 44, pp. 5365–76.
27. L.G. Hosamani: *Experimental and Theoretical Heat Transfer Studies in Vacuum Arc Remelting*, Oregon Graduate Institute of Science and Technology, USA, 1988.
28. L.G. Hosamani, W.E. Wood, and J.H. Devletian: *Metall. Appl.*, 1989, vol. 1989, pp. 49–57.